JOM, Vol. 76, No. 4, 2024
https://doi.org/10.1007/s11837-024-06395-8

TECHNICAL ARTICLE

Effect of Sintering Environment on Microstructures and Mechanical Properties of Metal Injection Molding Ti-6Al-4V Alloys

CHUANYONG LI,[1] LU LI,[1,2,6] WEICHEN ZHANG,[1] XIUHU GUO,[1] ZHENTAO YUAN,[3] XIAO WANG,[3] GANG CHEN,[4] and PENG CAO[5]

1.—Faculty of Material Science and Engineering, Kunming University of Science and Technology, Kunming 650093, People's Republic of China. 2.—Research Center for Analysis and Measurement, Kunming University of Science and Technology, Kunming 650093 People's Republic of China. 3.—City College, Kunming University of Science and Technology, Kunming 650051, People's Republic of China. 4.—Institute for Advanced Materials and Technology, University of Science and Technology Beijing, Beijing 100083 People's Republic of China. 5.—Faculty of Engineering, Chemical and Materials Engineering, University of Auckland, Private Bag 92019, Auckland 1142, New Zealand. 6.—e-mail: liluchina@kust.edu.cn

We employed a water-soluble binder to form Ti-6Al-4V alloy through metal injection molding and studied the effects of sintering (under Ar and various vacuum conditions) on the microstructure and mechanical properties of the material. The density was measured using the displacement method. The microstructure and mechanical properties of the alloy were characterized using optical microscopy, scanning electron microscopy, electron probe microanalysis, transmission electron microscopy and a universal testing machine. The results indicate that sintering the Ti-6Al-4V alloy under vacuum improved relative density and mechanical properties more than under the Ar environment. Furthermore, high-vacuum sintering significantly enhanced the relative density and mechanical properties of the material. At $< 10^{-3}$ Pa vacuum pressure, the material exhibited optimal relative density (97.6%), tensile strength (1022.7 MPa) and elongation (6.4%). Also, the impurity contents were 0.071%, 0.25% and 0.012% for carbon, oxygen and nitrogen, respectively, which met the impurity content requirements of Ti-6Al-4V alloy.

INTRODUCTION

Ti-6Al-4V (also known as Ti64) is a medium-strength $\alpha + \beta$ titanium alloy. It is perhaps the most widely used industrial titanium alloy. It possesses unique characteristics, such as high specific strength, excellent ductility, heat resistance, biocompatibility and excellent corrosion resistance.[1–3] It is extensively applied in various fields, including smart wearables, biomedical applications, transportation and aerospace.[4,5] Titanium's spring-back characteristics and relatively low thermal conductivity make it difficult to engineer and account for high processing costs associated with high material wastage associated with conventional machined and wrought products. For example, many aerospace applications involve removing $>$ 90% of the starting material during processing.[6] To mitigate these problems, the near-net-shaping (NNS) process [such as metal injection molding (MIM)] has been successfully used. In recent times, MIM has become an advanced manufacturing method for low-cost production of complex-shaped titanium and titanium alloy components.[7–10]

Moreover, metal injection molding involves mixing metal powders with binders to form granular feedstock followed by shaping the feedstock with an injection molding machine and then obtaining the desired products through debinding and sintering.[11–14] Nowadays, most researchers focus mainly

(Received September 29, 2023; accepted January 17, 2024; published online February 8, 2024)

on formulating binders in metal injection molding. For instance, Wang et al.[15] used a wax-based binder composed of 60% PW, 35% LDPE, and 5% SA homogenized with Ti-6Al-4V alloy powder for injection molding. While investigating its rheological properties, the authors found that the feedstock viscosity decreased with mixing time but increased with higher powder loading. A group of researchers from the University of Auckland[16] developed a novel ternary blend binder system consisting of 73% PEG, 20% PPC, 5% PMMA and 2% SA. Through capillary rheometry, thermogravimetry, Fourier-transform infrared spectroscopy and scanning electron microscopy, among other testing methods, they demonstrated that PMMA enhances the interaction between PEG and PPC, providing excellent homogeneity and rheological properties to the feedstock. In turn, a higher green strength of the compacted parts was maintained. However, there is limited research on sintering in metal injection molding.

While feedstock characteristics control final product quality, sintering crucially determines the product's microstructure, mechanical properties and physicochemical characteristics.[17,18] Titanium metal exhibits high reactivity, making it prone to carbide, nitride and oxide formations at ≈ 400°C. These impure phases reduce the sintering density, negatively affecting mechanical properties.[19–22] Therefore, titanium alloy sintering becomes crucial. Ergul et al.[23] sintered Ti-6Al-4V alloy under vacuum at various temperatures and durations. They found that sintering at 1270°C for 10 h resulted in the highest density (99%), with 704 MPa strength and 38.6 HRC hardness. Elsewhere, Limaberg et al.[24] studied the influence of the sintering environment and duration on the tensile properties and microstructure of Ti45Al5Nb0.2B0.2C alloy. They found that when sintered under argon atmosphere, the residual porosity of the samples increased with increasing argon gas pressure, from 0.1% at a vacuum level (10^{-3} Pa) to 1.1% (under 80 KPa argon protection). Likewise, Su et al.[25] investigated the influence of sintering temperature and subsequent hot isostatic pressing (HIP) on the microstructure and mechanical properties of Ti-6Al-4V alloy. The authors reported that vacuum sintering of the alloy induced many pores in the specimens. However, through subsequent hot isostatic pressing (HIP), the number of pores decreased. Among the HIP conditions, the fewest pores were observed when sintered at 1000°C. Under these conditions, the Ti-6Al-4V alloy formed a dense layer (290 μm thick), consisting of equiaxed grains with a 16 μm average size and 88.9% high-angle grain boundary fraction. This microstructure exhibited outstanding mechanical properties, with tensile strength of 1067 MPa and elongation of 17.5%. Tieyuan Bian et al.[26] prepared a high-oxygen-content Ti-6Al-4V alloy using a wax-based binder. The sintered samples contained needle-like α precipitates that severely reduced their ductility. Then, the samples were subjected to a rigorous heating cycle. The results revealed that heating inhibited the formation of needle-like α phases, increasing their elongation from 1.0% to 3.2%. For the sintering of Ti-6Al-4V alloy, most studies have focused on investigating the effects of sintering temperature and different heating regimes on the microstructure and properties. However, the impact of sintering environments on the microstructure and mechanical properties of injection-molded Ti-6Al-4V alloy has been rarely studied.

Therefore, the current research investigated metal injection molding (MIM) for preparing titanium alloy samples and studied the effects of the sintering environment on the microstructure and mechanical properties of Ti-6Al-4V alloy materials.

EXPERIMENTAL SECTION

Shandong Lianhong New Material Technology Co., Ltd., supplied the gas-atomized Ti-6Al-4V powder (D10 = 4.47 μm, D50 = 7.92 μm, D90 = 27.7 μm) used in this study. The SEM morphology of Ti-6Al-4V powder is shown in Fig. 1. The powder contains 0.0083% carbon (C), 0.095% oxygen (O) and 0.0065% nitrogen (N). We prepared a 90 mm × 5 mm dog bone-shaped tensile specimen via metal injection molding, as shown in Fig. 2. The binder was composed of polyethylene glycol, polymethyl methacrylate, polyoxymethylene and stearic acid. The powder loading capacity was 65 vol.%, injected using a molding machine. To debind, the green body was first immersed in distilled water at 40°C for 18 h. Then, it was dried in an oven at 50°C for 6 h. Thermal debinding was carried out at 500°C for 3 h using a vacuum atmosphere tube furnace (SK-G08163, Zhonghuan, Tianjin). Finally, the sample was heated at a rate of 10°C/min to 1200°C and held for 2 h, before cooling at 5°C/min to 700°C, and then allowed to cool to room temperature in the furnace. The entire sintering was conducted under Ar atmosphere, high vacuum (< 10^{-2} Pa) or ultra-high vacuum (< 10^{-3} Pa)

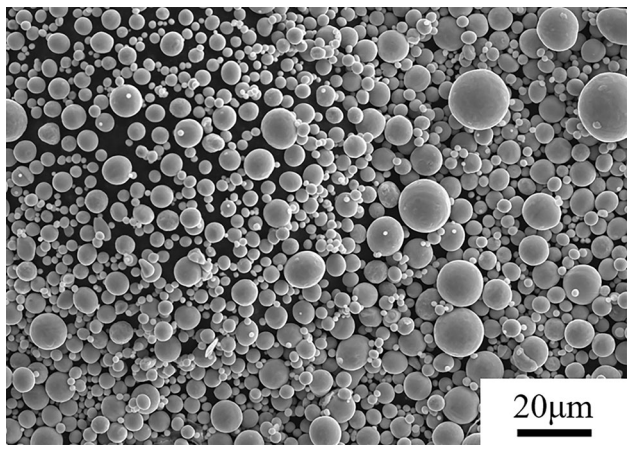

Fig. 1. SEM image of Ti-6Al-4V alloy powder.

environment. Figure 3 shows the titanium alloy injection molding process, while Fig. 4 represents the sintering temperature curve for Ti-6Al-4V alloy.

Using the Archimedes method, a density balance (MDJ-300S, LIHEN) measured the sintered samples' density. The middle rod-shaped portion of the sample was cut. The samples' elemental impurity content (such as O, N and C) was quantitated using the fusion extraction method on Leco ON736 and CS 744 elemental analyzers. Two ends of the sample were selected for microscopic structural analysis. The samples were polished and etched using Kroll's reagent (2.5 vol.% HNO_3 + 1.5 vol.% HCl + 1 vol.% HF + 95 vol.% H_2O) after grinding. The microstructure and elemental distribution of the samples were assessed using an optical microscope (OM, ECLIPSE MA200, Nikon), scanning electron microscope (SEM, VEGA3, TESCAN), transmission electron microscope (TEM, Tecnai G2 F20, FEI) and electron probe microanalyzer (EPMA-1720H, SHIMADZU). TEM samples were prepared through ion thinning with 5-kV ion beam voltage and 5° ion beam incident angle. Selected area electron diffraction (SAED) in TEM determined the crystal structure of the chosen phase, and the composition information of each phase was obtained through energy-dispersive X-ray spectroscopy (EDX). Furthermore, tensile tests were performed on the sintered samples using a universal testing machine (SHT4305, MTS) at a pulling rate of 1 mm/min. The data for each set of tensile properties represent the average of at least three samples.

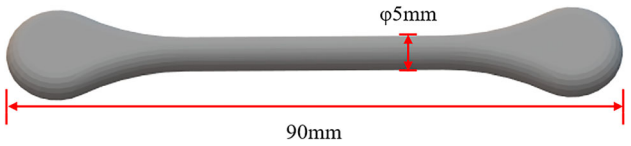

Fig. 2. Geometry of the green specimen.

RESULTS AND DISCUSSION

Elemental Impurity Content and Relative Density

Table I lists the impurity (C, N, O) concentrations and the relative densities of the samples under

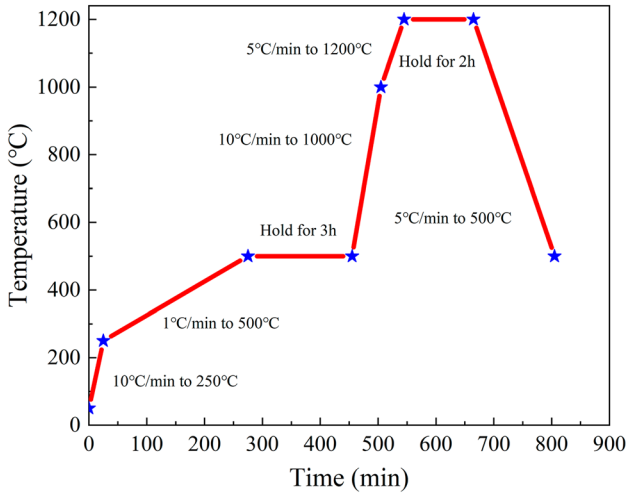

Fig. 4. Sintering process curve for Ti-6Al-4V alloy.

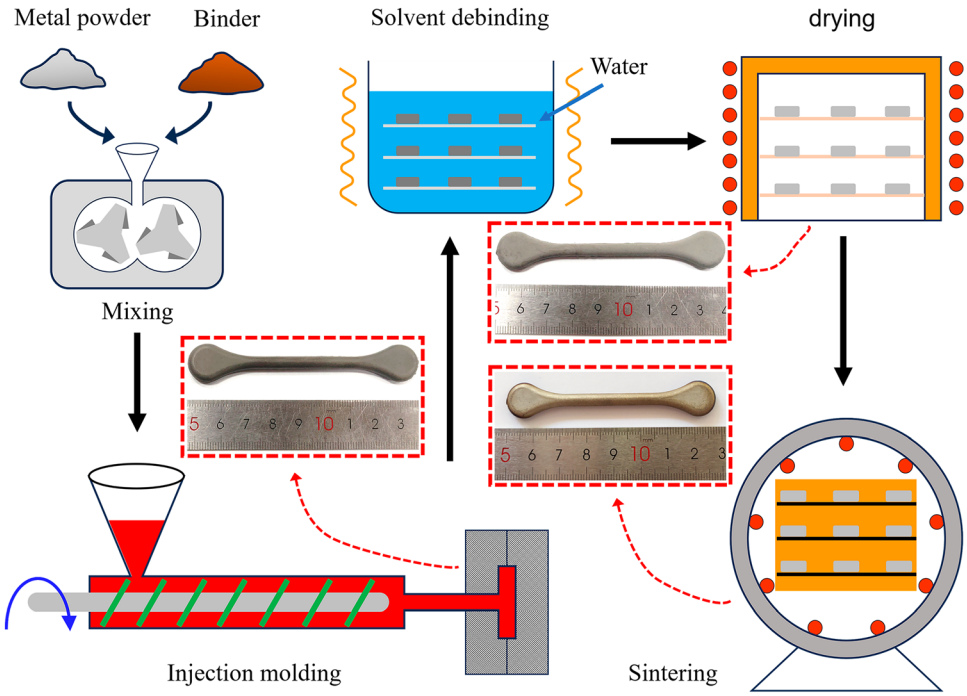

Fig. 3. Injection molding process flowchart for titanium alloy.

Table I. Impurity content and relative density of Ti-6Al-4V after sintering in argon and high vacuum environments

Sintering atmosphere	Oxygen (mass%)	Nitrogen (mass%)	Carbon (mass%)	Density (g/cm^3)	Relative density (%)
Ar atmosphere	0.889 ± 0.005	0.014 ± 0.002	0.088 ± 0.003	4.3103 ± 0.0022	97.3 ± 0.05
$< 10^{-2}$ Pa	0.360 ± 0.005	0.014 ± 0.002	0.068 ± 0.003	4.3192 ± 0.0022	97.5 ± 0.05
$< 10^{-3}$ Pa	0.25 ± 0.005	0.012 ± 0.002	0.071 ± 0.003	4.3237 ± 0.0022	97.6 ± 0.05

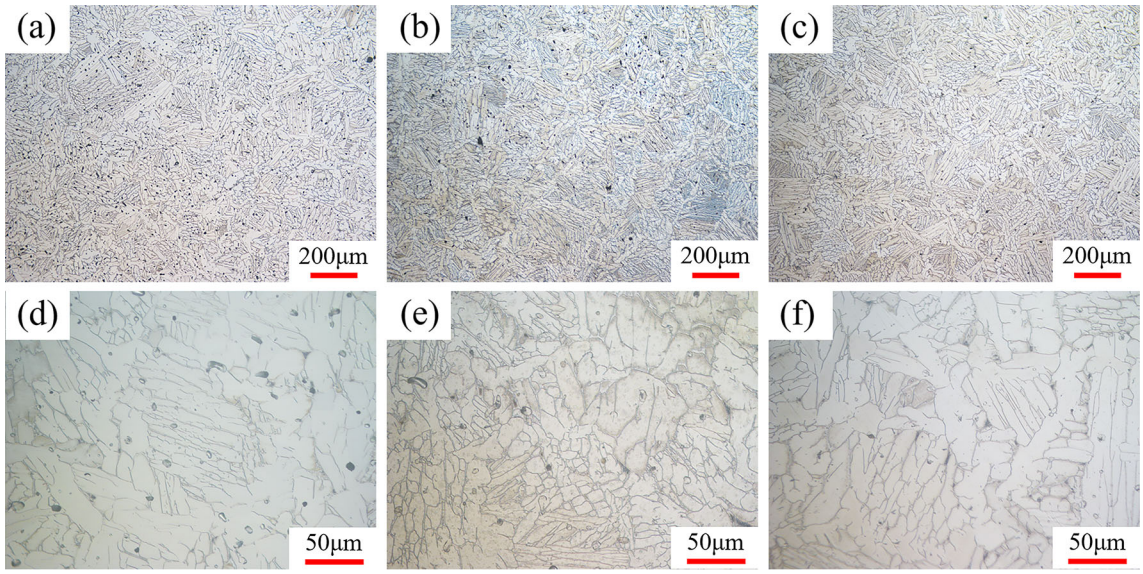

Fig. 5. Microstructures of Ti-6Al-4V under various sintering environments: (a) Ar atmosphere 100×; (b) high vacuum ($< 10^{-2}$ Pa) 100×; (c) high vacuum ($< 10^{-3}$ Pa) 100×; (d) Ar atmosphere 500×; (e) high vacuum ($< 10^{-2}$ Pa) 500×; (f) high vacuum ($< 10^{-3}$ Pa) 500×.

three sintering environments. Sintering under a high vacuum lowered the impurity concentrations more than under the Ar environment. As the vacuum level was increased, the O content decreased. Sintering under the Ar atmosphere increased the C and O content to 0.088% and 0.889%, respectively. However, sintering under a high vacuum ($< 10^{-3}$ Pa) lowered the C and O content to 0.071% and 0.25%, respectively. Compared to sintering in the Ar atmosphere, vacuum-environment sintering reduced the C and O content by 19.3% and 71.9%, respectively. At the same sintering temperature, high vacuum sintering resulted in a higher relative density than in the Ar environment. Ti-6Al-4V alloy, sintering under $< 10^{-3}$ Pa achieved a 97.6% relative density, whereas in Ar it reached 97.3%.

Microstructures

To further investigate the difference in relative density between sintering in Ar and high vacuum environments, the microstructure of Ti-6Al-4V alloy was investigated under three sintering conditions (Fig. 5). As Fig. 5 shows, all the samples exhibit typical microstructures of Ti-6Al-4V alloy irrespective of the sintering environment. The microstructure consists of small amounts of equiaxed α phase, intergranular β phase and lamellar α phase.[27]

Moreover, the number of pores increased with Ar atmosphere sintering than under the vacuum environment. This observation agrees with the density results. It could be attributed to the trapped residual Ar molecules in the pores during debinding. These trapped molecules hinder the closure of pores during sintering, forming numerous small pores. In contrast, sintering in a vacuum environment can remove gases within the pores and prevent the influx of external gases, thereby promoting pore shrinkage. From Fig. 5a, b, and c, we deduced that the number of pores induced by high vacuum sintering was significantly the lowest of the three conditions. However, some pores were still formed.

Figure 6 displays SEM images of the three sintered samples, showing the pore morphology. Based on their appearance, the pore can be categorized into irregular pores (the red regions) and relatively regular pores (the yellow regions) in Fig. 6.

Forming these pore types is attributed to the heat distribution during sintering. Irregular pores were

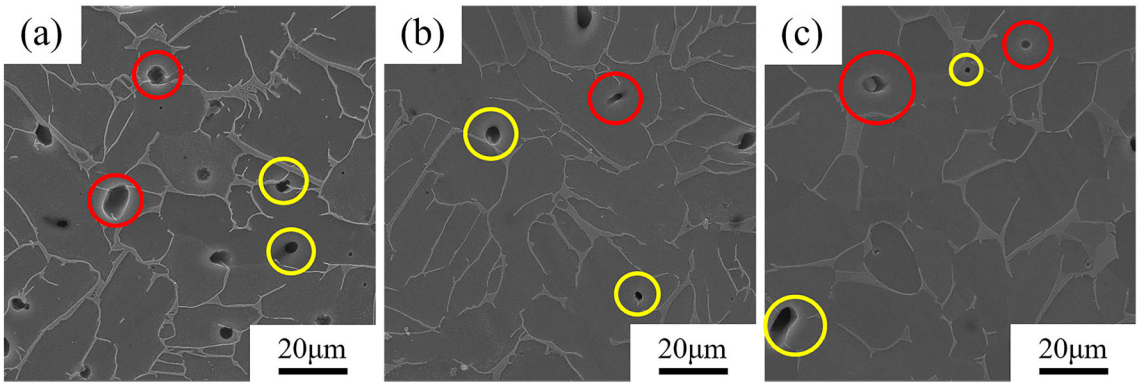

Fig. 6. SEM images of Ti-6Al-4V alloy under different sintering environments: (a) Ar atmosphere; (b) high vacuum (< 10^{-2} Pa); (c) high vacuum (< 10^{-3} Pa) (Color figure online).

typically located at the sintering necks. In a densely packed powder compact, localized contacts occurred between the powder particles, forming sintering necks. As the sintering progressed, a minute liquid phase was generated in this region, rounding the sintering necks. Due to the mutual diffusion of the powder particles, some of the gas trapped on the surface and in the gaps of the powder entered the liquid phase. Under the influence of surface tension, pores are formed, and they remain within the sample during solidification.[28] Irregular pores, which are generally closed pores caused by exogenous gases, cannot be easily eliminated through deformation during processing. After undergoing deformation under external forces, the pores were distorted because of the compression of the surrounding tissue. The inner surfaces of the deformed pores could have undergone stress concentration, leading to crack initiation, detrimental to the material's overall performance. This observation confirmed that when sintering in an Ar environment, Ar or other gases trapped on the powder surface are more likely to enter the liquid phase, ultimately forming more pores during solidification.

On the other hand, the interior of the regular pores was usually in a vacuum state. These pores were primarily distributed in unfilled regions after material shrinkage, formable at any part of the sintered body. Since their interior was in a vacuum state, the pores could be eliminated by deformation during processing. During deformation, the pore walls made contact with each other, underwent mutual diffusion and bonded under external forces. Their structure was similar to those of dense materials, so they usually did not significantly affect the material's performance. This observation also indicates that the relative density and mechanical properties of the sintered samples were improved through hot isostatic pressing, resulting in denser materials with enhanced mechanical performance.[25]

Figure 7 characterizes the elemental distribution of Ti-6Al-4V alloy under three sintering environments using EPMA. Figure 7a, b, and c depicts similar distributions of Al and V contents in Ti-6Al-4V alloy after sintering in the three environments. For the three samples, the sintering temperature was set at 1200°C, surpassing the β-phase transition temperature. While slowly cooling the alloy, the α phase continuously precipitated at the β grain boundaries. Al and V are stabilizing elements for the α and β phases, respectively. When the β phase was transformed into the α phase, V was crucial for the solid-solution strengthening of β-Ti, preventing the complete transformation of the β phase into α phase. At the same time, Al helped stabilize the α phase in the titanium alloys. This observation is consistent with Al and V content distributions (Fig. 7a, b, and c) where Al and V were enriched in the α and β phases, respectively.

As shown in Fig. 7a, sintering in Ar reveals enriched O and C within the microstructure, while N is distributed haphazardly in the structure. In contrast, sintering under high vacuum (Fig. 7b and c) resulted in relatively lower C and O contents. Also, under high vacuum, C exhibited partial enrichment, but O was nearly absent. To further investigate the presence and distribution of C and O in the microstructure, a detailed analysis via TEM was done.

Figure 8 shows the TEM images of the α-Ti and β-Ti interfaces. The dark, striped regions in Fig. 8a represent β-Ti, while the remaining area corresponds to α-Ti. Fourier transformation and diffraction spot calibration were performed on the high-resolution morphology of the α-Ti and β-Ti interfaces (Fig. 8c). We observed that the following orientation relationships existed between α-Ti and β-Ti:

$$[1\,1\,-2\,-3]\,\alpha-\mathrm{Ti}\|[1\,-1\,-1]\,\beta-\mathrm{Ti}(-1\,0\,1\,-1)\alpha-\mathrm{Ti}\|(-1\,-1\,0)\,\beta-\mathrm{Ti}$$

Upon observation, we found that the (− 1 0 1 − 1) α-Ti crystal plane was nearly parallel to the (− 1 − 1 0) β-Ti crystal plane. The interplanar spacing in α-Ti on the (− 1 0 1 − 1) crystal plane was 2.091 nm, while it was 2.263 nm in the β-Ti on the (− 1 − 1 0)

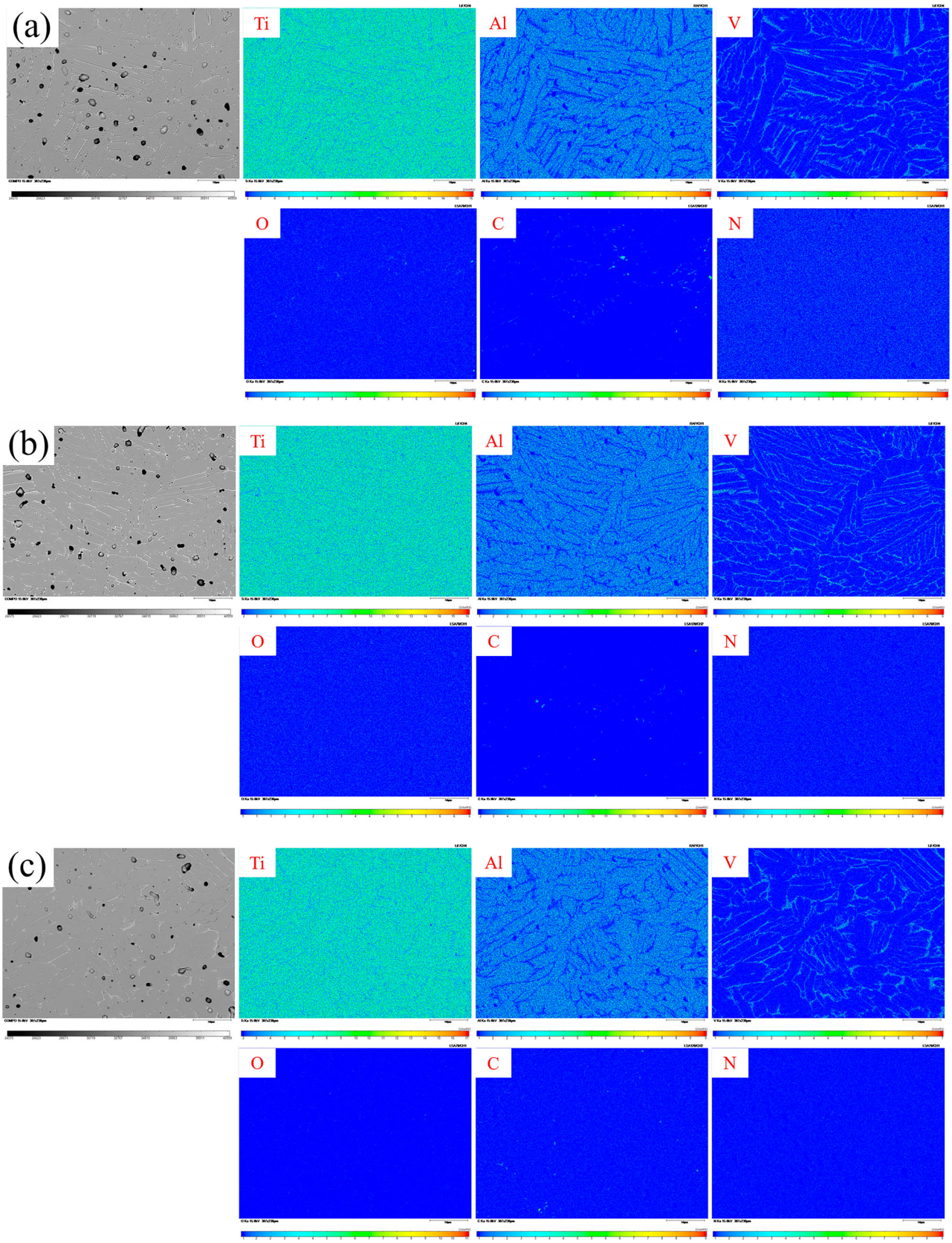

Fig. 7. EPMA images of elemental distribution in Ti-6Al-4V alloy under three sintering environments: (a) Ar atmosphere; (b) high vacuum ($< 10^{-2}$ Pa); (c) high vacuum ($< 10^{-3}$ Pa).

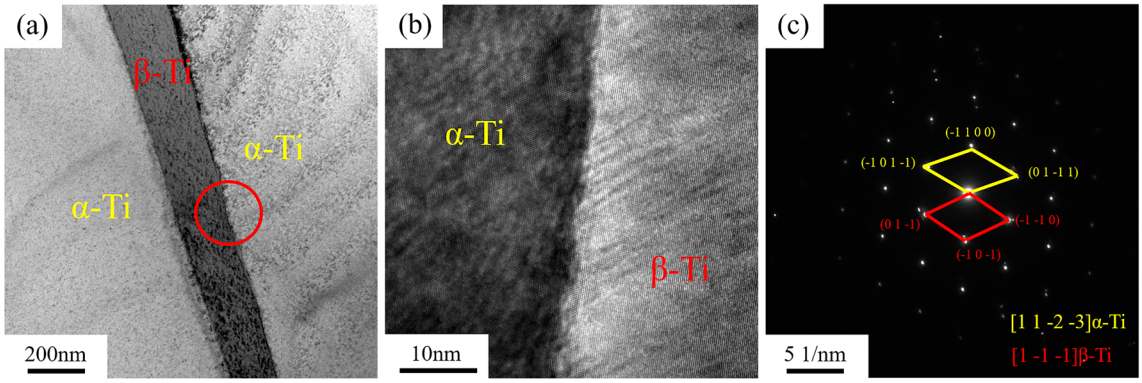

Fig. 8. Transmission electron microscope images: (a) distribution of β-Ti in α-Ti; (b) α-Ti/β-Ti interface; (c) Fourier transform pattern of α-Ti/β-Ti interface.

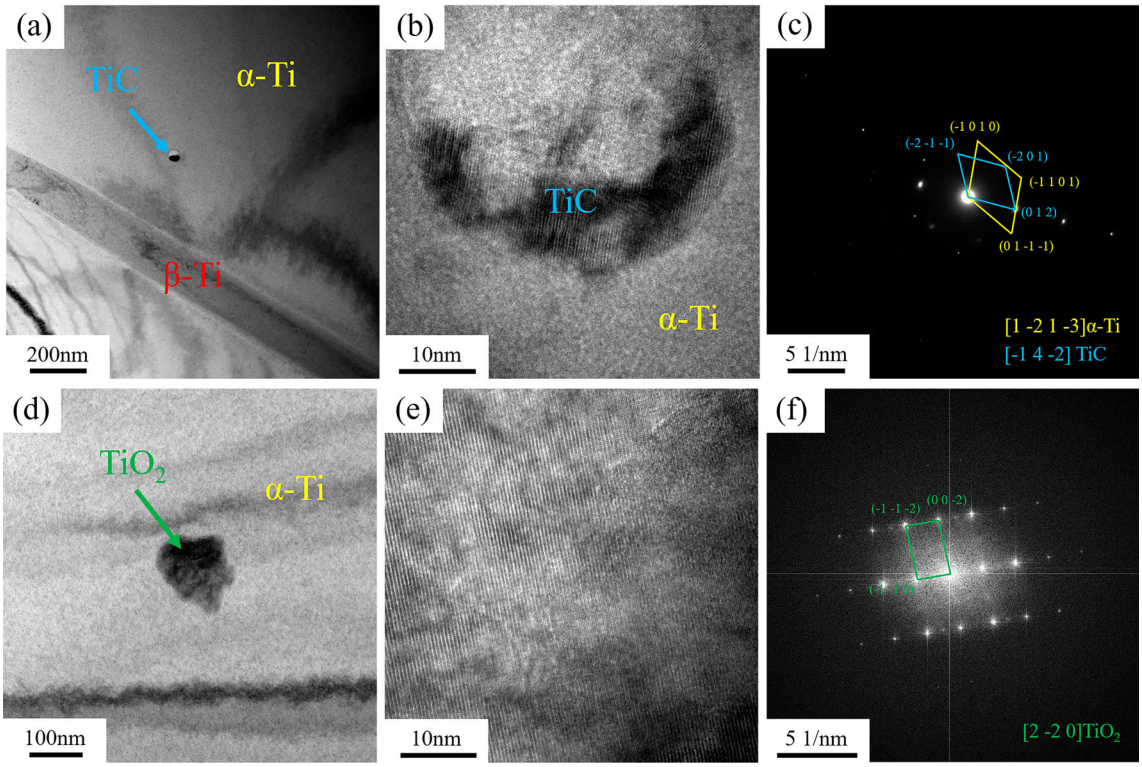

Fig. 9. Transmission electron microscope images: (a) distribution of TiC particles in α-Ti; (b) TiC/α-Ti interface; (c) Fourier transform pattern of TiC/α-Ti interface; (d) distribution of TiO_2 in α-Ti; (e) high-resolution image of TiO_2 particle; (f) Fourier transform pattern of TiO_2 particle.

crystal plane. We calculated the mismatch between these specific orientation relationships as 8.2%, indicating the presence of a semi-coherent relationship between α-Ti and β-Ti.

The TEM micrographs of the sintered sample in an argon gas environment are shown in Fig. 9. They reveal that α-Ti contains spherical particles and black block-like features, respectively (Fig. 9a and d). A high-resolution examination of the spherical particles and black block-like features evidenced a precipitate phase within the α-Ti matrix (Fig. 9b). The Fourier transformation and diffraction spot calibration performed on the high-resolution morphology of the precipitate phase and its interface with α-Ti (Figure 9c) confirmed the precipitate phase as TiC. Furthermore, a high-resolution examination, Fourier transformation and diffraction spot calibration in Fig. 9e identified the black block-like features as the TiO_2 phase (Fig. 9f).

Through TEM analysis, we observed that TiO_2 was not present in the high vacuum condition samples, whereas TiC particles were present in the $< 10^{-3}$ Pa environment sample. This observation could be attributed to the fact that in the Ar atmosphere, some gas within the pores of the sample could not be fully expelled through the

flowing Ar, resulting in the residual oxygen in the sample. The elevated oxygen content (0.889 wt.%) resulted in a rapid reaction between oxygen and titanium to generate titanium oxide at temperatures $> 600°C$. In contrast, in a vacuum environment, it is advantageous for eliminating residual gases within the pores as well as reaction gas by-products, resulting in a lower oxygen content (0.25 wt.%). Oxygen reacts with Ti only at the surface (not likely at the inner layer of the metal), forming a dense oxide layer.[29] Simultaneously, the lower oxygen partial pressure contributed to reducing oxidation, and TiO_2 was not detectable. At elevated temperatures, carbon readily reacts with titanium to produce TiC. Due to the presence of binders in the green specimen, organic compounds decompose during the thermal debinding process, potentially leaving some residual carbon unremoved in the pores of the samples. Consequently, as the sintering temperature rises, the reaction between carbon and titanium occurs. However, the residual carbon content is very low (0.071–0.088 wt.%), and we have only detected TiC in the sample under a $< 10^{-3}$ Pa environment.

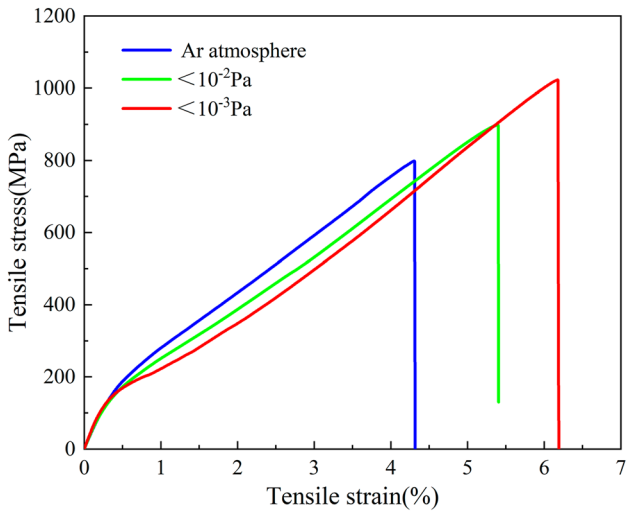

Fig. 10. Engineering stress-strain curves of Ti-6Al-4V alloy samples obtained from tensile tests under three sintering environments.

Mechanical Properties

The tensile properties of Ti-6Al-4V alloy under the three sintering environments are shown in Fig. 10. As the vacuum level was increased, the material's tensile strength and elongation improved. Under Ar atmosphere, the tensile strength was 798.5 MPa, with a 4.3% elongation When the vacuum level reached $< 10^{-3}$ Pa, the material's tensile strength and elongation were 1022.7 MPa and 6.4%, respectively. Compared to sintering in Ar, the tensile strength and elongation increased by 28.1% and 48.8%, respectively.

The inferior mechanical properties of the sintered samples under the Ar environment could be attributed to their lower relative density and higher porosity. When testing for tensile strength, stress concentration regions were readily formed at the pore edges, making it prone to crack initiation and propagation, thereby significantly reducing the alloy's strength and fracture elongation.

Figure 11 indicates that the Ti-6Al-4V alloy samples exhibited ductile fracture surfaces under the three sintering environments. In the Ar environment (Fig. 11a), the fracture surface displays cleavage steps adjacent to the flat cleavage plane. There were dimples, indicating localized plastic deformation during the tensile test, which corresponds to a quasi-cleavage fracture with relatively poor plasticity, consistent with its mechanical properties. On the other hand, under high vacuum conditions, the fracture surfaces of the samples exhibit larger dimples, indicative of ductile fracture with improved plasticity (Fig. 11b and c). Figure 11 also reveals voids on the fracture surfaces, regardless of the sintering environment, confirming that

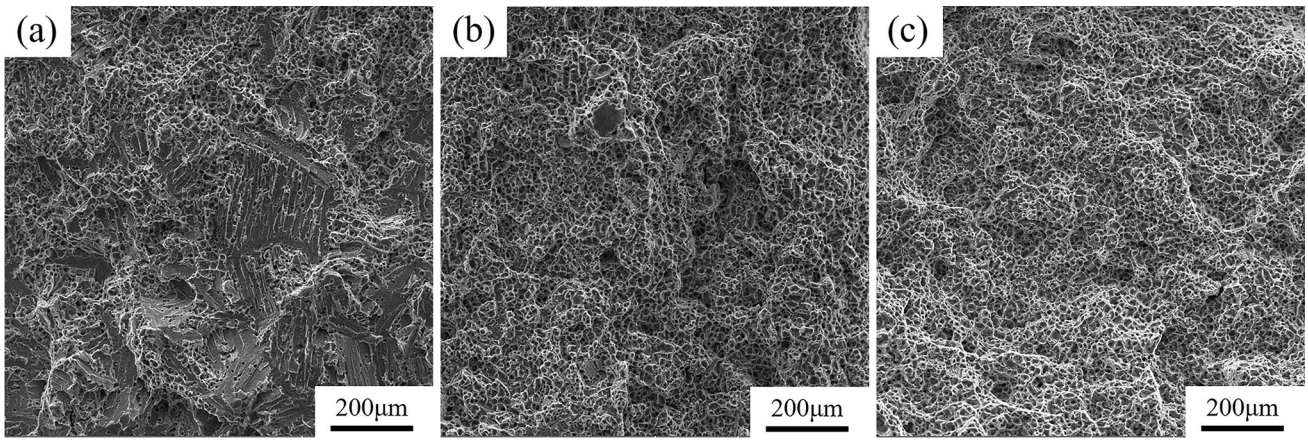

Fig. 11. SEM images of fracture surfaces of Ti-6Al-4V alloy under three sintering environments: (a) Ar atmosphere; (b) high vacuum ($< 10^{-2}$ Pa); (c) high vacuum ($< 10^{-3}$ Pa).

the overall relative density of all three samples remained relatively low.

CONCLUSION

The following conclusions are derived from the current study:

1. Ti-6Al-4V alloy sintered under various environments showed the highest relative density and lowest impurity content under the high vacuum (10^{-3} Pa) environment, with a relative density of 97.6% and impurity C and O contents of 0.071% and 0.25%, respectively.
2. By sintering under the Ar environment, TiC and TiO_2 were formed in the microstructure, while in the high vacuum (10^{-3} Pa) sintering environment, only TiC particles were found.
3. Sintering in the high vacuum (10^{-3} Pa) environment yielded the best mechanical properties for Ti-6Al-4V alloy, with a 1022.7 MPa tensile strength and a 6.4% elongation, whereas in the Ar atmosphere, the values were only 798.5 MPa and 4.3%.

ACKNOWLEDGEMENTS

The authors gratefully acknowledge the support of Key Research and Development Project of Yunnan Province and International Science and Technology Cooperation Project (202103AF140004), Technology Talent and Platform Plan (202305AQ350001) and Key Research and Development Project of Yunnan Province (202203AM140010). This work is supported by the National and Local Joint Engineering Laboratory of Advanced Metal Solidification Forming and Equipment Technology, and Joint Laboratory for Key Technologies of Titanium Forming, Kunming University of Science and Technology, Kunming, China.

CONFLICT OF INTEREST

The authors declare that they have no known competing financial interests or personal relationships that could have appeared to influence the work reported in this paper.

REFERENCES

1. A. Kaouka, and K. Benarous, *J. Mater. Res. Technol.* 8, 6407 (2019).
2. S. Mironov, Y.S. Sato, and H. Kokawa, *J. Mater. Sci. Technol.* 34, 58 (2018).
3. Y. Fu, N. Guo, L. Zhou, Q. Cheng, and J. Feng, *Mater. Des.* 186, 108284 https://doi.org/10.1016/j.matdes.2019.108284 (2020).
4. S. Bootchai, N. Taweejun, A. Manonukul, and C. Kanchanomai, *J. Mater. Eng. Perform.* 29, 4559 (2020).
5. Y. Yan, E. Chibowski, and A. Szcześ, *Colloids Surf. A Physicochem. Eng. Aspects* 510, 135 (2016).
6. J.A.D. Oliveira, S.L.M.R. Filho, C.H. Lauro, and L.C. Brando, *Int. J. Adv. Manuf. Technol.* 92, 1 (2017).
7. P. Xu, F. Pyczak, W. Limberg, R. Willumeit-Rmer, and T. Ebel, *Mater. Des.* 211, 110141 (2021).
8. N.N. Mahmud, F.A.A. Azam, M.I. Ramli, F.M. Foudzi, and A.B. Sulong, *J. Mater. Res. Technol.* 11, 2255 (2021).
9. A. Dehghan-Manshadi, D. Stjohn, M. Dargusch, Y. Chen, J.F. Sun, and M. Qian, *J. Manuf. Process.* 31, 416 (2018).
10. M.F.F.A. Hamidi, W.S.W. Harun, M. Samykano, S.A.C. Ghani, Z. Ghazalli, F. Ahmad, and A.B. Sulong, *Mater. Sci. Eng., C* 78, 1263 https://doi.org/10.1016/j.msec.2017.05.016 (2017).
11. A. Romero, and G. Herranz, *Powder Technol.* 308, 472 https://doi.org/10.1016/j.powtec.2016.12.055 (2017).
12. M. Subaşi, A. Safarian, and Ç. Karataş, *Int. J. Adv. Manuf. Technol.* 105, 4747 https://doi.org/10.1007/s00170-019-04514-3 (2019).
13. A. Dehghan-Manshadi, M.J. Bermingham, M.S. Dargusch, D.H. StJohn, and M. Qian, *Powder Technol.* 319, 289 https://doi.org/10.1016/j.powtec.2017.06.053 (2017).
14. T. Deguchi, M. Ito, A. Obata, Y. Koh, T. Yamagishi, and Y. Oshida, *J. Dent. Res.* 75, 1491 https://doi.org/10.1177/00220345960750070901 (1996).
15. J.H. Wang, Q.N. Shi, C.L. Wu, and J. Xi, *Trans. Nonferrous Met. Soc. China* 23, 2605 (2013).
16. M.D. Hayat, P.P. Jadhav, H. Zhang, S. Ray, and P. Cao, *Powder Technol.* 330, 304 https://doi.org/10.1016/j.powtec.2018.02.043 (2018).
17. G. Thavanayagam, K.L. Pickering, J.E. Swan, and P. Cao, *Powder Technol.* 269, 227 (2015).
18. K.K. Rane, P.P. Date, G.N. Kotwal, K.C. Nayak, and T.S. Srivatsan, *Mater. Manuf. Process.* https://doi.org/10.1080/10426914.2022.2157432 (2022).
19. Y. Xia, Z.Z. Fang, D. Fan, P. Sun, Y. Zhang, and J. Zhu, *Int. J. Hydrogen Energy* 43, 11939 https://doi.org/10.1016/j.ijhydene.2018.03.170 (2018).
20. B. Bergmann, B. Denkena, and F. Schaper, *CIRP J. Manuf. Sci. Technol.* 45, 253 https://doi.org/10.1016/j.cirpj.2023.06.016 (2023).
21. R. Banoth, R. Sarkar, A. Bhattacharjee, T.K. Nandy, and G.V.S. Nageswara Rao, *Mater. Des.* 67, 50 https://doi.org/10.1016/j.matdes.2014.11.004 (2015).
22. J. Guo, Y. Shi, C. Li, and G. Zhang, *Surf. Coat. Technol.* 418, 127254 https://doi.org/10.1016/j.surfcoat.2021.127254 (2021).
23. E. Ergül, H. Özkan Gülsoy, and V. Günay, *Powder Metall.* 52, 65 https://doi.org/10.1179/174329008X271691 (2009).
24. W. Limberg, T. Ebel, F. Pyczak, M. Oehring, and F.P. Schimansky, *Mater. Sci. Eng., A* 552, 323 https://doi.org/10.1016/j.msea.2012.05.047 (2012).
25. S. Su, Z. Hong, Y. Wu, P. Wang, X. Li, J. Wu, and Y. Huang, *Int. J. Adv. Manuf. Technol.* 126, 3861 https://doi.org/10.1007/s00170-023-11376-3 (2023).
26. T. Bian, C. Ding, X. Yao, J. Wang, W. Mo, Z. Wang, P. Yu, and S. Ye, *Mater. Sci. Eng., A* 840, 142924 https://doi.org/10.1016/j.msea.2022.142924 (2022).
27. Y. Chong, T. Bhattacharjee, and N. Tsuji, *Mater. Sci. Eng., A* 762, 138077 https://doi.org/10.1016/j.msea.2019.138077 (2019).
28. J. Bidulská, R. Bidulský, M. Actis Grande, and T. Kvačkaj, *Materials*. https://doi.org/10.3390/ma12223724 (2019).
29. K. Aniołek, *Vacuum* 144, 94 https://doi.org/10.1016/j.vacuum.2017.07.023 (2017).